

Noninvasive Internal Body Thermometry With On-Chip GaAs Dicke Radiometer

Joeeun Lee^{ID}, *Graduate Student Member, IEEE*, Gabriel Santamaria Botello^{ID}, *Member, IEEE*, Robert Streeter^{ID}, *Graduate Student Member, IEEE*, and Zoya Popovic^{ID}, *Fellow, IEEE*

Abstract—In this letter, we present an on-chip radiometer for noninvasive internal body temperature measurements. The switch and low-noise, high-gain amplifier parts of the Dicke radiometer are designed as a single monolithic microwave integrated circuit (MMIC) using enhancement-mode $0.1\ \mu\text{m}$ GaAs pseudomorphic high electron mobility transistor (pHEMT) technology. The radiometer shows 45 dB of gain and 0.88 dB noise figure (NF) at 1.4 GHz. When connected to a near-field antenna probe, measurements are obtained on a skin-muscle phantom to track the muscle temperature. The near-field antenna is designed to receive blackbody radiation from the 15 mm thick muscle phantom under the 2 mm thick skin phantom. To retrieve the subcutaneous temperature of the muscle, a radiometer calibration is performed with a reference noise source by switching at 10 Hz. The integration time of the measurements is 2 s. A 27-MHz bandwidth results in an average measurement error of 0.77 K compared to a thermocouple measurement of the muscle phantom performed 30 s before the radiometric measurement.

Index Terms—GaAs monolithic microwave integrated circuit (MMIC), low noise amplifier, phantom tissue, radiometer, single-pole double-throw (SPDT) switch, thermometer.

I. INTRODUCTION

THE acquisition and long-term monitoring of internal tissue temperature is a valuable metric with benefits across the medical space. For instance, artificial hypothermia is needed for an emergency cardiac repair surgery, during which the blood supply is interrupted. However, a smooth return to normothermia is required within only 30 min. Brain temperature is monitored throughout this procedure to ensure proper temperature maintenance, currently with nasal catheters [1]. On a more widely applicable basis, the monitoring of muscle temperature in first-responders, athletes, and military personnel can help prevent heat-related injuries and optimize athletic performance [2], [3]. Furthermore, the diagnosis of sleep disorders is related to body core temperature [4] and tracking internal temperature can assist with sleep disorder treatment. Tissue temperature is an indicator of not only infection, but also healing for burn patients [5]. Joint inflammation

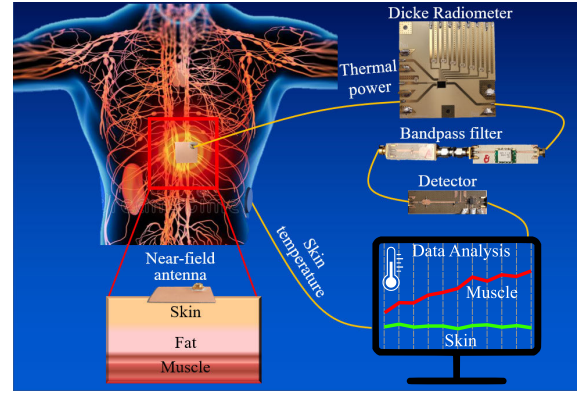


Fig. 1. Illustration of noninvasive internal body thermometry with a microwave radiometer placed below the sternum [10]. A near-field antenna is placed on the skin to receive thermal power from a stack of tissue layers. This signal is transferred to a low-noise receiver, and the output is processed with a temperature estimation algorithm. A thermocouple on the skin provides additional information to the algorithm.

detection additionally depends on reliable tissue temperature measurements [6].

Currently, there is no commercially available wearable device that can noninvasively measure temperature at a few cm depths in the body. Magnetic resonance imaging (MRI) can give indirect relative measurements with high resolution, but it is large and expensive. Heat flux devices can be wearable, but their usability outside clinical or laboratory settings remains limited [7]. A method that has been shown in the literature is using microwave radiometry in the 1–3 GHz range, e.g., [8], [9] where the tissue sensing depth is on the order of cm. However, the thermal power $P = kTB$ received with a measurement bandwidth B on the order of tens of MHz, is very low, in the $-100\ \text{dBm}$ range for normal human temperatures. Therefore, radiometer receivers need to have high gain and low noise. The approach in this letter is shown in Fig. 1, a near-field antenna attached to the outer skin receives thermal power from a stack of tissue layers. These data are amplified by the Dicke radiometer, and then the power detector converts the data to be used for calibrated temperature analysis. A separate thermocouple on the skin allows the estimation of the temperature of the inner tissue layers. The radiometer design and temperature retrieval are described in this letter.

II. RADIOMETER OVERVIEW

A key metric for a radiometer is the minimal detectable temperature difference, ΔT , which depends on the hardware and is described by a noise temperature T_{sys} , the measurement bandwidth B , and the integration time τ [11]. For the total

Manuscript received 21 February 2023; revised 3 April 2023 and 4 April 2023; accepted 5 April 2023. The work of Joeeun Lee was supported by the National Science Foundation under Award IIP 2044668. (Corresponding author: Joeeun Lee.)

The authors are with the Department of Electrical, Computer, and Energy Engineering, University of Colorado at Boulder, Boulder, CO 30309 USA (e-mail: joeeun.lee@colorado.edu; gabriel.santamariabotello@colorado.edu; robert.streeter@colorado.edu; zoya.popovic@colorado.edu).

This article was presented at the IEEE MTT-S International Microwave Symposium (IMS 2023), San Diego, CA, USA, June 11–16, 2023.

Color versions of one or more figures in this letter are available at <https://doi.org/10.1109/LMWT.2023.3265806>.

Digital Object Identifier 10.1109/LMWT.2023.3265806

TABLE I
COMPARISON OF RADIOMETER ARCHITECTURES

	Dicke [8]	Correlation [12]	Hybrid [13]
ΔT	$2T_{sys}/\sqrt{\tau B}$	$\sqrt{2}T_{sys}/\sqrt{\tau B}$	$2T_{sys}/\sqrt{\tau B}$
Pros	– Gain fluctuation calibrated	– No switch loss – 100% duty cycle	– No switch loss – Gain fluctuation calibrated
Cons	– Sensitive to input impedance – Limited time on target	– Duplicate components – Sensitive to phase balance	– Duplicate components – Limited time on target

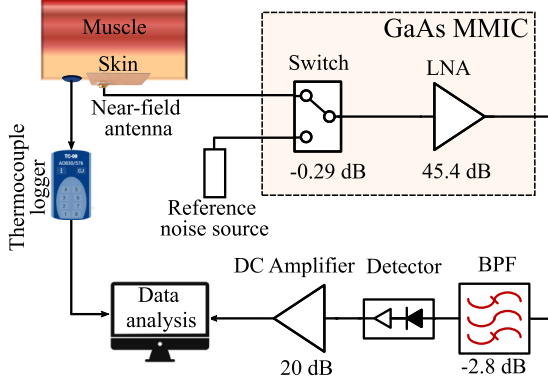


Fig. 2. Block diagram of a Dicke radiometer connected to a phantom tissue stack of skin and muscle. The Dicke switch and LNA are implemented on a GaAs MMIC and followed by off-chip bandpass filter, detector, and dc amplifier. The output is digitized and processed for temperature retrieval. A thermocouple logger monitors skin temperature.

power radiometer, the resolution is given by

$$\Delta T = \frac{T_{sys}}{\sqrt{\tau B}}$$

but this simple architecture, consisting of a low-noise amplifier (LNA), filter, and detector, is susceptible to drift and fluctuations and cannot be calibrated while operating. Other radiometer architectures include the Dicke radiometer, correlation radiometer, and a combination of the two, which we refer to as the “hybrid.” A Dicke radiometer uses a switch to allow calibration against a known thermal source at the expense of 50% duty cycle of the measurement [11]. Table I shows a summary of the achievable ΔT , as well as the *pros* and *cons* of various architectures. In this letter, we show an implementation of a Dicke architecture, chosen due to its simplicity and the fact that human temperature changes on a scale much slower than the required switching period.

Fig. 2 shows the block diagram of the Dicke radiometer. A near-field antenna is designed to effectively receive blackbody radiation from a buried tissue layer. It couples the total radiometric power received from all tissue layers to a switch that alternates between the tissue stack and a known noise reference in order to calibrate for gain fluctuations. The LNA gain is selected to meet a link budget, and is followed by broadband and narrowband bandpass filters. The detector converts the amplified thermal noise input to a dc voltage. At the output of the post-detection amplifier, the voltage from a room-temperature source is on the order of 10 mV. After taking into account the detector responsivity, loss in the filters, switch loss, and cable loss with near-field antenna mismatch, a requirement for the LNA gain is found to be ≥ 45 dB,

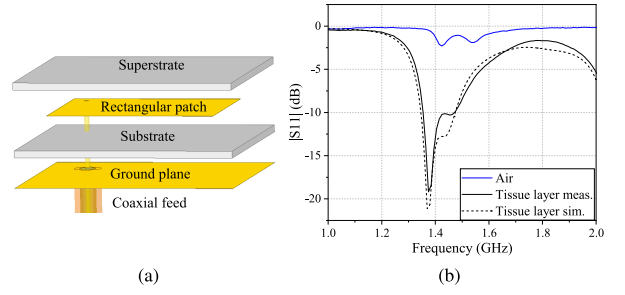


Fig. 3. (a) Cross section of the near-field antenna designed for thermal power retrieval, with a high sensing coefficient from the muscle phantom layer. (b) Simulated and measured reflection coefficient magnitude when the near-field antenna is placed on to the phantom tissue stack. The measured reflection coefficient is also shown for the antenna in free space for comparison.

assuming a room-temperature input power of -100 dBm in a 27-MHz bandwidth of the 1.4 GHz quiet band. The overall receiver noise figure (NF) is primarily determined by the LNA first stage NF and loss of the switch. The design of the radiometer components is given next.

III. MMIC DICKE RADIOMETER DESIGN

In this section, the design of the radiometer components is described, starting from the near-field antenna, followed by the GaAs monolithic microwave integrated circuit (MMIC) switch integrated with a three-stage LNA.

A. Near-Field Antenna

For receiving blackbody radiation from a subcutaneous tissue layer, a near-field antenna different from a free-space radiator is designed. The goal is to receive as much power as possible from the muscle layer under the skin layer in this case. A 2 mm skin phantom ($\epsilon_r = 28$, $\sigma = 0.82$ S/m) from [14] is placed on top of a plastic bag filled with saline solution ($\epsilon_r = 77.7$, $\sigma = 1.26$ S/m) used as a muscle phantom, approximating the values given in [15]. The muscle phantom is kept in a water bath with a temperature controller to set the temperature to a known value for characterizing the radiometer accuracy.

A coaxial-fed rectangular patch is designed by simulations in Ansys HFSS using the above properties of the muscle phantom with dimensions 6×6 cm and 1.5 cm thickness, surrounded by air. A 1.27 mm thick Rogers RO3010 material is used for the substrate and superstrate, Fig. 3(a). The resulting size of the rectangular metal patch is 42×40 mm² for operation at 1.4 GHz, and its simulated and measured reflection coefficient magnitude is shown in Fig. 3(b). The comparison with the antenna measured in air clearly shows that it is designed to be matched to a specific tissue stack.

B. Switch and LNA Design

Fig. 4(a) illustrates the circuit schematic of an absorptive single-pole double-throw (SPDT) switch and a three-stage LNA implemented in the 110 nm PIH1-10 WIN Semiconductors GaAs process. The SPDT switch uses a shunt-series topology for high isolation. The inductor between the shunt and series transistors is used to create a resonance with the parasitic capacitance of the *off* transistors, improving the insertion loss and isolation of the switch. The resonating inductor also biases all the nodes in the switch, avoiding extra loss and voltage drop from biasing resistors. Fig. 5 shows the

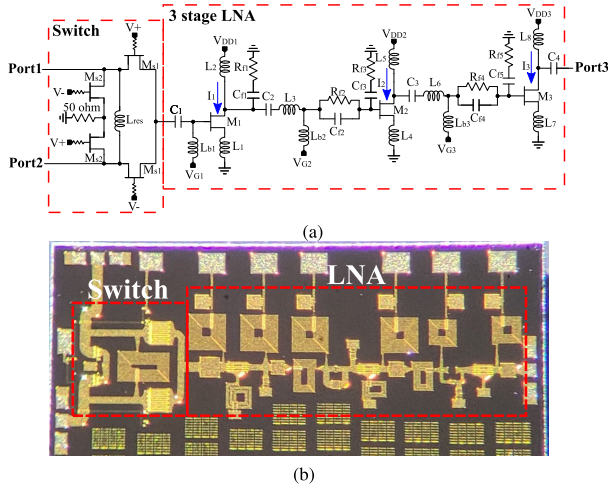


Fig. 4. (a) Circuit schematic and (b) photograph of the GaAs MMIC SPDT switch and a three-stage LNA. The total chip dimensions are 3.75×1.7 mm.

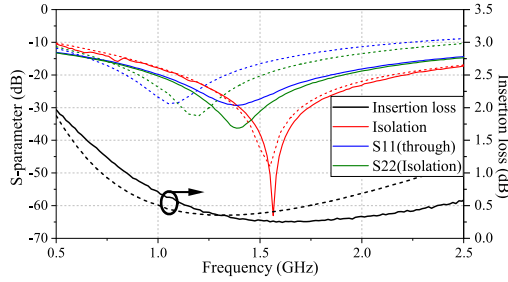


Fig. 5. Measured (solid line) and simulation (dashed line) performance of an MMIC SPDT switch.

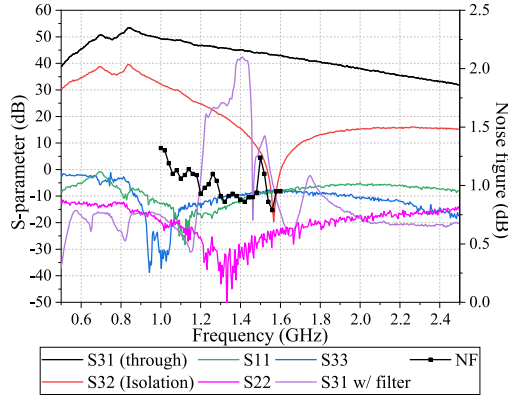


Fig. 6. Measured S -parameter magnitudes of the packaged SPDT switch and LNA MMIC front end of the Dicke radiometer. A coaxial calibration is performed on the connector reference planes.

switch performance. The minimum insertion loss is 0.24 dB at 1.61 GHz, and the maximum isolation is 63 dB at 1.58 GHz. At the design frequency of 1.4 GHz, the insertion loss is 0.29 dB and the isolation is 30.8 dB. The dimensions of the switch alone are 0.9×0.9 mm.

A three-stage LNA is designed to achieve >45 dB gain at 1.4 GHz [16]. Stability is crucial for an LNA with high gain. Therefore, five distributed low-pass and high-pass filters are used at interstage nodes to ensure stability and minimize NF degradation. Fig. 6 shows the S -parameter measurements of the LNA together with the SPDT switch. The gain of the through ports at 1.4 GHz is 45.1 dB and the isolation [transmission between ports 2 and 3 in Fig. 4(a)] is 15.5 dB. The NF of the through port is 0.88 dB at 1.4 GHz. To reduce out-of-band interference, an off-chip bandpass filter is connected

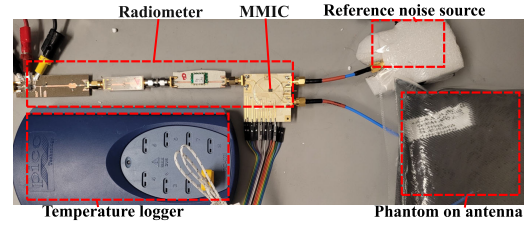


Fig. 7. Photograph of test setup for temperature measurement. Hot and cold muscle phantoms are alternated and placed on top of the skin phantom, with the near-field antenna underneath and not visible in the photograph.

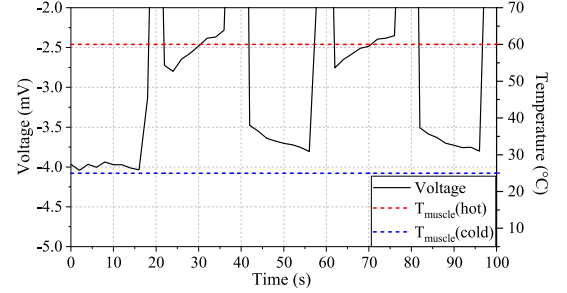


Fig. 8. Measured calibrated output of the detector when hot (60°C) and cold (25°C) muscle phantoms are placed on the skin phantom and alternated for about 20 s. The output voltage increases with the hot muscle phantom, as expected. The spikes around 20, 40 s, etc., are periods when the muscle phantoms are being alternated and the antenna is not behaving as designed.

to the output of the MMIC. Including the filter loss, the gain is 41.9 dB. The dimension of the LNA is 2.6×1 mm. For biasing and convenient connections, the MMIC is packaged on a 45×45 mm printed circuit board (PCB) board.

IV. MEASUREMENTS AND TEMPERATURE ESTIMATION

Temperature measurements are done using the radiometer and the near-field antenna on the tissue phantom, as shown in Fig. 7. Two bags of saline muscle phantom are used; one is a hot phantom at 60°C , and the other is a cold phantom kept at room temperature, 25° . These two phantoms are placed alternately on the skin phantom. Fig. 8 shows the measured output dc voltage of the radiometer. With the cold muscle phantom, the radiometer shows lower voltage than with the heated muscle phantom, as expected. For these measurements, the radiometer is calibrated against a reference noise source, in this case, a $50\text{-}\Omega$ temperature-controlled coaxial load.

From the measured output voltage level on a sampling oscilloscope, a temperature retrieval algorithm is used to estimate the temperature of the muscle. The radiometer measures the total noise temperature from the skin and muscle phantom, and ambient. Assuming the ambient contribution is negligible (validated by simulations), the total radiometric temperature can be written as a weighted sum

$$T_{\text{total}} = W_{\text{skin}} T_{\text{skin}} + W_{\text{muscle}} T_{\text{muscle}}$$

where the coefficients W_i are found from the percentage of noise power from each of the two separate layers, calculated by integration of the volume loss power density using reciprocity as in [9]. Fig. 9 shows the simulated volume Joule loss of the antenna and tissue stack simulated in transmission with 1 W of input power at the probe feed. The coefficients are found as the ratio of the Joule loss in a particular volume to the total Joule loss and the values are shown in Fig. 9. The temperature of the skin phantom, T_{skin} is known since it is

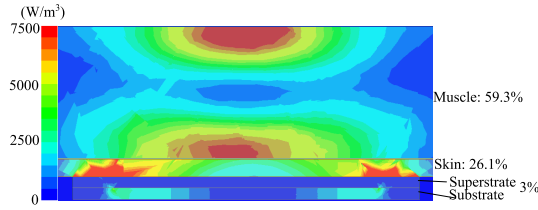


Fig. 9. Full-wave simulations of volume Joule loss density (W/m^3) of the near-field antenna on a skin-muscle phantom with 1 W at the feed. The weighting coefficients (percentages of total power) are also stated, with 3% of the total power being in the surrounding air and unaccounted for here.

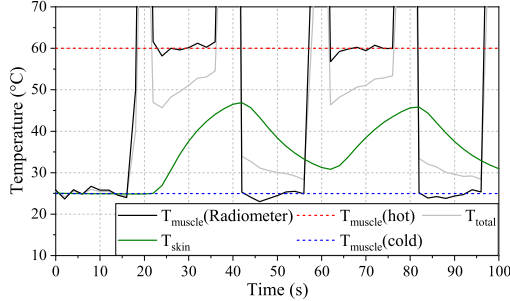


Fig. 10. Measured temperature of the muscle tissue phantom, using T_{skin} (green line) measured by a thermocouple and subtracted in the algorithm. The red and blue dotted lines show the temperatures of the water bath used to set the known phantom temperature, 60° and 25°.

measured by an individual thermocouple placed on the skin. The temperature of the muscle T_{muscle} is calculated from the above equation, and Fig. 10 shows T_{muscle} compared to the actual known temperature of the saline phantom. The average error is 0.77 °C and the maximum error is 3.2 °C.

V. CONCLUSION

This letter demonstrates a switch and stable 45-dB gain LNA GaAs MMIC with an NF of 0.88 dB at 1.4 GHz, showing for the first time that a radiometer for internal body temperature can be miniaturized by MMIC integration. The power consumption of this radiometer is about 80 mW, compared to ≥ 0.5 W for a similar device with off-the-shelf components.

ACKNOWLEDGMENT

The authors would like to thank WIN Semiconductors and Dr. D. Danzilio for circuit fabrication as a part of a graduate course at the University of Colorado Boulder, Boulder, CO, USA.

REFERENCES

- [1] F. Biancari, T. Juvonen, and G. Speziale, "Commentary: Cooling the brain for elective aortic hemiarch repair," *J. Thoracic Cardiovascular Surg.*, vol. 165, no. 5, pp. 1774–1775, May 2023.
- [2] C. L. Lim, C. Byrne, and J. K. Lee, "Human thermoregulation and measurement of body temperature in exercise and clinical settings," *Ann. Acad. Med., Singap.*, vol. 37, no. 4, pp. 347–353, Apr. 2008.
- [3] A. S. Howe and B. P. Boden, "Heat-related illness in athletes," *Amer. J. Sports Med.*, vol. 35, no. 8, pp. 1384–1395, Aug. 2007.
- [4] L. C. Lack, M. Gradisar, E. J. W. Van Someren, H. R. Wright, and K. Lushington, "The relationship between insomnia and body temperatures," *Sleep Med. Rev.*, vol. 12, no. 4, pp. 307–317, Aug. 2008.
- [5] A. Y. Owda, N. Salmon, S. Shylo, and M. Owda, "Assessment of bandaged burn wounds using porcine skin and millimetric radiometry," *Sensors*, vol. 19, no. 13, p. 2950, Jul. 2019.
- [6] V. M. Ravi, A. K. Sharma, and K. Arunachalam, "Pre-clinical testing of microwave radiometer and a pilot study on the screening inflammation of knee joints," *Bioelectromagnetics*, vol. 40, no. 6, pp. 402–411, Sep. 2019.
- [7] S. Mendt et al., "Circadian rhythms in bed rest: Monitoring core body temperature via heat-flux approach is superior to skin surface temperature," *Chronobiol. Int.*, vol. 34, no. 5, pp. 666–676, May 2017, doi: [10.1080/07420528.2016.1224241](https://doi.org/10.1080/07420528.2016.1224241).
- [8] S. G. Vesnin et al., "Portable microwave radiometer for wearable devices," *Sens. Actuators A, Phys.*, vol. 318, Feb. 2021, Art. no. 112506.
- [9] P. Momenroodaki, W. Haines, M. Fromandi, and Z. Popovic, "Non-invasive internal body temperature tracking with near-field microwave radiometry," *IEEE Trans. Microw. Theory Techn.*, vol. 66, no. 5, pp. 2535–2545, May 2018.
- [10] Maya0851601054. (Jul. 2021). *3D Rendering Illustration of Lymphatic System Stock Illustration*. [Online]. Available: <https://www.dreamstime.com/d-rendering-illustration-lymphatic-system-orange-lymphatic-system-front-view-image225146687>
- [11] F. T. Ulaby et al., *Microwave Radar and Radiometric Remote Sensing*, vol. 4, no. 5. Ann Arbor, MI, USA: Univ. of Michigan Press, 2014.
- [12] E. Villa, N. Arteaga-Marrero, G. León, L. F. Herrán, I. Mateos, and J. Ruiz-Alzola, "A 3.5-GHz pseudo-correlation type radiometer for biomedical applications," *AEU - Int. J. Electron. Commun.*, vol. 130, Feb. 2021, Art. no. 153558. [Online]. Available: <https://www.sciencedirect.com/science/article/pii/S143484112032762X>
- [13] J. Lee, G. S. Botello, R. Streeter, K. Hall, and Z. Popović, "A hybrid correlation-dicke radiometer for internal body thermometry," in *Proc. 52nd Eur. Microw. Conf. (EuMC)*, Sep. 2022, pp. 464–467.
- [14] *Customized Generic Phantoms*. Accessed: Dec. 1, 2022. [Online]. Available: <https://speag.swiss/components/phantoms/customized-2/customized-generic-phantoms-2/>
- [15] D. Andreuccetti, R. Fossi, and C. Petrucci, *Calculation of the Dielectric Properties of Body Tissues in the Frequency Range 10 Hz–100 GHz*. Accessed: Dec. 1, 2022. [Online]. Available: <http://niremf.ifac.cnr.it/tissprop/htmlclie/htmlclie.php>
- [16] J. Lee and Z. Popović, "A GaAs LNA MMIC for a correlation-Dicke radiometer internal-body temperature sensor," in *Proc. IEEE Radio Wireless Symp. (RWS)*, Jan. 2023, pp. 31–33.